Biomaterials Translational

Living hybrid material based on probiotic with photothermal properties inhibits PD-L1 expression after tumouricidal photothermal therapy

Ning Jiang[1], Mingyan Jiang[2], Jianshu Chen[1], Ali Mohsin[1], Yuqing Mu[3], Xiaoping Yi[1], Yingping Zhuang[1], Jiangchao Qian[1], Jiaofang Huang[1,2,]*

Key Words:
biomaterials; *Escherichia coli* Nissle 1917; programmed cell death ligand 1; photothermal therapy

From the Contents

ABSTRACT

Photothermal therapy is a safe and effective tumour treatment strategy due to its excellent spatiotemporal controllability. However, interferon gamma in the tumour microenvironment is upregulated after photothermal therapy, which enhances the expression of programmed cell death ligand 1 (PD-L1) in tumour cells. This further promotes immunosuppression and tumour metastasis, resulting in a poor prognosis in cancer therapy. Traditional nanodrugs often face challenges in penetrating the dense extracellular matrix of solid tumours, whereas certain probiotics possess the ability to specifically colonise the core regions of tumours. In this research, we used Escherichia coli Nissle 1917 (ECN) as a chassis cell and self-assembly polydopamine (PDA) on the ECN surface. The black PDA@ECN (notes as PE) actively colonises at the tumour site and produces a photothermal effect under 808 nm laser irradiation to kill tumour cells. To overcome the high expression of PD-L1 induced after photothermal therapy, metformin (MET) was also encapsulated in PE to form PDA@MET@ECN (notes as PME). In vivo experiments demonstrated that PME effectively inhibited the PD-L1 expression and growth of CT26 tumour cells. Overall, PME reverses the immunosuppressive tumour microenvironment and enhances the effect of photothermal/immune therapy in tumour treatment.

***Corresponding author:**
Jiaofang Huang,
huangjf@ecust.edu.cn.

http://doi.org/10.12336/biomatertransl.2025.01.006

How to cite this article:
Jiang, N.; Jiang, M.; Chen, J.; Mohsin, A.; Mu, Y.; Yi, X.; Zhuang, Y.; Qian, J.; Huang, J. Living hybrid material based on probiotic with photothermal properties inhibits PD-L1 expression after tumouricidal photothermal therapy. *Biomater Transl.* **2025**, *6*(1), 73-84.

Introduction

In recent years, the concept of precision medicine has gradually emerged in tumour treatment. Photodynamic therapy and photothermal therapy (PTT) have attracted significant attention in oncology for their outstanding localised treatment effectiveness and minimal side effects.[1] Generally, photosensitisers (PIs) accumulate at tumour sites via blood circulation, and these PIs remain non-toxic under normal conditions. However, when excited by laser of a specific wavelength, PIs convert laser energy into cytotoxic agents, such as reactive oxygen species and heat.[2] Photodynamic therapy and PTT exhibit excellent spatiotemporal controllability due to their laser excitation at specific wavelengths, which results in minimal side effects.[3] On the other hand, PTT can directly burn tumour cells, thereby largely avoiding the emergence of drug resistance in tumour cells. However, free PIs are difficult to accumulate at the tumour site. For example, U.S. Food and Drug Administration-approved PI indocyanine green (ICG) is metabolised by the liver and kidneys and excreted within just 30 minutes after entering the body.[4] Drug delivery strategies based on nanoparticles not only enhance the stability of PIs but also extend their blood circulation time, increasing their accumulation at the tumour site.[5] Unfortunately, the dense extracellular matrix and

high microenvironmental osmotic pressure of solid tumours hinder these nanoparticle-encapsulated PIs from accumulating within tumours.[6-8] Consequently, it is imperative to address the challenge of optimising the accumulation and infiltration of PIs at tumour sites.

PTT can damage tumour cells, induce tumour immunogenic cell death, and release related antigens such as calprotectin (CRT), adenosine triphosphate, and high mobility group protein to recruit immune cell infiltration at the tumour site.[9] PTT often induces acute inflammation at the tumour site, leading to the expression of programmed cell death ligand 1 (PD-L1) on tumour cells through the interferon gamma (IFN-γ) signalling pathway.[10] The high expression of PD-L1 on the surface of tumour cells not only suppresses immune cell activity through the programmed cell death protein 1 (PD-1)/PD-L1 signalling axis, achieving an "immune brake", but also helps tumour cells escape immune surveillance, enabling metastasis.[11, 12] To address immune evasion after PTT, researchers have combined PTT with PD-L1 monoclonal antibodies to inhibit tumour growth, resulting in notable therapeutic outcomes.[13] However, the high cost of PD-L1 antibodies significantly increases treatment expenses, limiting their widespread use. Besides, clinical data indicate that some patients do not respond to PD-L1 antibody therapy. Therefore, there is an urgent need to develop drug delivery platforms that specifically inhibit PD-L1 expression.

A recent report has shown that the physiological environment of tumour cells is significantly different from normal physiological conditions, known as the tumour microenvironment.[14] Due to uncontrolled growth and metabolism of tumour cells, the tumour microenvironment is characterised by hypoxia, mild acidity, and immune suppression, which favour the growth and proliferation of certain microorganisms, such as *Escherichia coli* Nissle 1917 (ECN)[15] or *Salmonella*.[16] As research progresses, scientists have discovered that ECN can specifically colonise tumour sites due to its facultative anaerobic nature.[17] Therefore, researchers have developed chemical modification,[18, 19] surface coating,[20, 21] and other techniques to load drugs onto the surface of ECN as a drug delivery carrier.[22] Compared to ordinary nanoparticles, the live drug delivery strategy based on ECN significantly enhances drug accumulation at the tumour site.[18] Additionally, ECN can effectively penetrate the dense extracellular matrix and high osmotic pressure of solid tumours, reaching deep into the tumour core, thereby achieving a therapeutic effect.[23-25] It has been reported that dopamine (DA) can self-assemble into black polydopamine (PDA) nanoparticles. These nanoparticles exhibit excellent photothermal properties and have been validated in a mouse tumour model. Moreover, DA can self-assemble on the surface of ECN, forming a PDA coating with photothermal capabilities. The resulting PDA@ECN (notes as PE) can penetrate deep into the core of solid tumours, enhancing the penetration ability of PIs at tumour sites.

To overcome the dense extracellular matrix of solid tumours and enhance the penetration capability of PIs at tumour sites, we employed ECN as a chassis cell and PDA on its surface to construct PE with photothermal potential. Considering the immune escape of tumour cells after PTT, we encapsulated metformin (MET) on the surface of PE (PDA@MET@ECN, notes as PME) to inhibit the expression of PD-L1 on tumour cells after PTT (**Figure 1**). CT26 mouse tumour models showed that PME can specifically accumulate at tumour sites, and its excellent photothermal properties inhibit tumour cell growth. Moreover, the experimental results further proved that PME effectively inhibits PD-L1 expression in CT26 cells, and extends the lifespan of mice. The PME delivery strategy enhances the application of photothermal immunotherapy in tumour treatment.

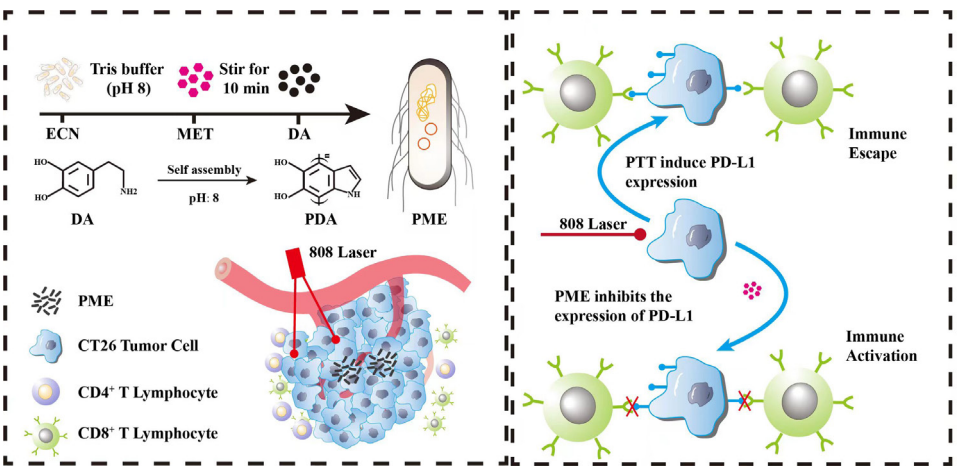

Figure 1. The synthesis route of PME and the mechanism of enhancing the anti-tumour effect by PTT and inhibition PD-L1 expression in the tumour microenvironment. Created with Adobe Illustrator 2019. DA: dopamine; ECN: *Escherichia coli* Nissle 1917; MET: metformin; PDA: polydopamine; PD-L1: programmed cell death ligand 1; PME: PDA@MET@ECN; PTT: photothermal therapy.

1 State Key Laboratory of Bioreactor Engineering, East China University of Science and Technology, Shanghai, China; 2 College of Life Sciences, Jiangxi Normal University, Nanchang, Jiangxi Province, China; 3 Institute for biomedicine and glycomics, Griffith University School of Medicine and Dentistry, Griffith University, Queensland, Australia

Methods

Cells and animals

Murine colon cancer CT26 cells (CBNumber: CB75525505) were provided by Wenzhou Medical University. These cells were cultured in Dulbecco's modified Eagle medium (Gibco-BRL, Grand Island, NY, USA) supplemented with 10% foetal bovine serum (Gibco-BRL) (Grand Island, NY, USA) and 1% penicillin/streptomycin at 37°C under 5% CO_2.

Balb/c female mice (5-6 weeks) were purchased from Animal Experimental Center of JSJ Company (Shanghai, China). All procedures strictly complied with the ethical and legal requirements under the Administration Committee of Experimental Animals in Shanghai and were approved by Animal Ethics Committee of East China University of Science and Technology.

Construction and characterisation of PME

ECN (Xi'an Jiaotong University, Xi'an, China) was inoculated into LB medium and cultured at 37°C, 220 r/min. When the optical density at 600 nm reached 0.8, the ECN was centrifuged at 4500 r/min for collection and washed three times with phosphate buffered saline (PBS; Beyotime, Shanghai, China). The ECN was resuspend in Tris-HCl to a concentration of 1×10^8 colony-forming units (cfu)/mL, the 100 μL of MET solution (10 mg/mL) was added, and stirred for 5 minutes, then added 100 μL of DA solution (10 mg/mL) and continued stirring at room temperature for 10 minutes. After the reaction, the samples were washed three times with Tris-HCl and stored at 4°C for later use.

PME was washed three times with deionised water and then fixed with 2.5% glutaraldehyde solution for 2 hours at 4°C. The samples were then dehydrated using ethanol solutions of increasing concentrations (50%, 80%, 85%, 90%, 95%, and 100%) for 10 minutes each at room temperature. After dehydration, the samples were dried and observed using a scanning electron microscope (JEM-F200, Japan).

Briefly, PME (1×10^8) was collected by centrifugation at 4500 r/min and rinsed three times with an aqueous solution. Then, 10 μL of the sample was applied to a copper mesh (BZ10024a, ZhongMirror Instrument, Shanghai, China) and left for 1 minute. Following this, the mesh was stained with 1% uranyl acetate for 30 seconds, then rinsed three times with deionised water. After drying, the sample was photographed using a transmission electron microscope (JME-1400).

The prepared PME was dissolved in 1 mL of deionised water. The zeta potential and particle size was measured by Malvern particle size analyzer (Mastersiser 3000+, Malvern Panalytical Ltd., Malvern, UK).

Stability and drug release behaviour of PME

0.1 mL of PME was dissolved in PBS, Tris-HCl, or PBS containing 10% foetal bovine serum, respectively. After vortexing, it was stored at 4°C, and sampled at pre-set time points. The particle size was measured.

1 mL of PME was then added to a dialysis bag (molecular weight cutoff: 3 kDa). The dialysis bag was placed in a beaker with 30 mL of different buffers, and stirred at 300 r/min at room temperature. At pre-designed time points, 0.2 mL of solution was removed from the beaker and added fresh buffer to maintain the total volume at 30 mL. The collected samples were placed in a quartz cuvette and ultraviolet-visible spectroscopy (Lambda 25, PerkinElme, Shelton, CT, USA) was used for detection.

Photothermal ability of PME

200 μL of PME at different concentrations was added to a 96-well plate and was irradiated with an 808 nm laser (0.5 W/cm²) for different times. A hand-held thermal imager was used to measure the temperature in the wells. Additionally, the temperature rise was monitored and recorded during irradiation. After 5 seconds of laser irradiation, the laser was removed and the temperature was monitored continuously until it stabilised. The laser heating process was repeated for 5 seconds three times.

Induction of CRT expression in CT26 cells by PME

CT26 cells were placed at 1×10^5 cells/well in 3 cm² confocal dishes. After 12 hours, the cells were treated with PBS, PM (PDA@MET), PE, or PME at a drug concentration of 5×10^7 cfu/mL (MET: 0.5 mg). After 2 hours of drug treatment, the cells were irradiated with an 808 nm laser for 10 seconds. Aftrer 6-hour incubation, the cells were fixed with 4% paraformaldehyde (Beyotime), and then incubated with Alex-594-labelled anti-CRT antibody (mouse, 1:2000, Abways, Cat# CY5353) at 4°C for 2 hours. The cells were stained with 4',6-diamidino-2-phenylindole (Beyotime) at room temperature for 10 minutes and washed three times with PBS. The CRT was detected with confocal laser scanning microscope (Nikon, Japan).

Inhibition of PD-L1 expression by PME

CT26 cells were plated in 24-well plates at (5×10^4) cells per well and incubated overnight. The fresh medium was replaced with PBS, PM, PE, or PME (MET: 0.5 mg/mL; ECN: 5×10^7 cfu/mL) and incubated for 4 hours. The cells were irradiated with an 808 nm laser for 10 seconds each and incubated for 6 hours. The cells were lysed on ice with radio immunoprecipitation assay lysis buffer (Beyotime) containing 1% phenylmethanesulfonyl fluoride to collect the denatured proteins and perform sodium dodecyl sulfate-polyacrylamide gel electrophoresis with 10% gels. The proteins were transferred to a cellulose membrane and blocked. The samples were incubated with anti-PD-L1 antibody (mouse, Affinity, Cat# BF8035) at 4°C overnight, followed by secondary antibody incubation, and the relative protein expression was observed using a gel imaging system (TAITAN, Shanghai, China).

Cytotoxicity of CT26 cells

CT26 cells were plated in 96-well plate at 1×10^4 cells per well. After 12 hours, fresh Dulbecco's modified Eagle medium containing different concentrations of PM, PE, or PME was added followed by incubation for 24 hours and then the cell viability was detected using Cell Counting Kit-8 (Beyotime).

CT26 cells were planted in 96-well plates at 1×10^4 cells per

well. After 12 hours, fresh Dulbecco's modified Eagle medium containing different concentrations of PM, PE, or PME was added followed an irradiation with an 808 nm laser for 10 seconds and continued to incubate for another 12 hours. Finally, the cell viability was detected.

CT26 cells were plated in 24-well plate at 3×10^4 cells per well and incubated overnight. The medium was replaced with fresh Dulbecco's modified Eagle medium containing PM, PE, or PME. After 12 hours of incubation, the cells were irradiated with a laser and continued to incubate for 12 hours. Cells were collected and stained using a live/dead cell staining kit (Beyotime), and observed by confocal laser scanning microscope.

Construction of mouse tumour model

Balb/c mice were used to construct a subcutaneous tumor model. Briefly, 0.2 mL of CT26 cells (1×10^7 cells/mL) was injected into the left forelimb armpit of each mouse. The tumour growth was observed after 1 week. When the tumour volume reached 100 mm^3, the mice was used for subsequent experiments. Tumour volume was calculated as long diameter × (short diameter)^2/2.

In vivo metabolic behaviour of PME

The tumour-bearing mice were randomly divided into two groups, with tail vein injection of PDA@ICG and PDA@ICG@ECN (1×10^7 cfu/mouse), respectively. After injection, the drug distribution was observed by a small animal *in vivo* imaging system (PerkinElner FMT4000, USA), and the fluorescence intensity at the tumour site was analysed by ImageJ 6.0 (National Institutes of Health, Bethesda, MD, USA).

In vivo photothermal effect of PME

The tumour-bearing mice were randomly divided into two groups, and intravenous injected with PBS or PME. After 24 hours, the tumour site was irradiated with an 808 nm laser for 2 minutes and the temperature change was recorded using a handheld thermal imager. The temperature at tumour site was maintained at 45°C. Mice were anesthetized with tribromoethanol at a dose of 0.2 mL per 10 g of body weight. After anesthesia, the mice were euthanised by spinal dislocation. The tumour tissue was grinded and soaked in PBS, placed 10 μL of the soaking solution on LB agar plates, and cultured overnight at 37°C. The colony formation was observed.

CT26 cell growth *in vivo*

The mice were randomly divided into eight groups: PBS, PM, PE, and PME (MET: 5 mg/kg; ECN: 1×10^7 cfu/mL) with or without laser treatment. After 24 hours of treatment, the tumour site was irradiated with an 808 nm laser for 15 seconds for three times. The body weight and changes in tumour volume were observed at 14 days.

Immune cell infiltration

The mouse tumour tissues were embedded in OCT glue and stored at –20°C. A cryostat (PerkinElner) was used to section. Then the sections were incubated with different antibodies (CD4, Abways, Cat# CY5392; CD8, Abways, Cat# CY5219; KI67, Abways, Cat# CY5219) for 1 hour at room temperature, and then incubated for 1 hour with FITC (Cat# AB0121) or AF-594 (Cat#AB0151) secondary antibody. After staining, the section was observed using a confocal laser scanning microscope.

Enzyme-linked immunosorbent assay

After various treatments, blood from the mice was collected into 1.5 mL centrifuge tubes via the retro-orbital method. The blood was then centrifuged at 4°C (1500 × g, 10 minutes) to collect the serum, which was kept on ice. Finally, the detection was performed using a kit from Merun Biotech (MA1364-1; Shanghai, China).

Safety detection

After 14 days of treatment, mouse blood was collected, and the liver and kidney function, including aspartate aminotransferase, alanine aminotransferase, creatinine, and blood urea nitrogen was detected using kits from Nanjing Jiancheng (Nanjing, China). Major organs and tumour tissues were collected for haematoxylin and eosin staining and observed under a microscope.

Statistical analysis

GraphPad Prism 7.0 software (GraphPad Software, Boston, MA, USA, www.graphpad.com) was used to statistical analysis. Quantitative data are presented as mean ± standard deviation (SD), acquired from three independent parallel trials unless otherwise specified. The results were analyzed by two-tail Student's *t*-test or one-way analysis of variance. $P < 0.05$ was designated as statistically significant.

Results

PME is successfully constructed and has an excellent viability of photothermal capability

DA can polymerise on the surface of ECN in an alkaline buffer solution, forming a coating with photothermal properties.[26, 27] To determine successful construction of PME, we first used scanning electron microscope to examine the morphology of ECN before and after PDA modification. As shown in **Figure 2A** and **Additional Figure 1**, the surface of wild-type ECN exhibited a smooth cellular structure. However, after PDA modification, the surface of PME showed spherical structures, which might be nanoparticles formed by DA on the ECN surface. Further observation with transmission electron microscope revealed many PDA nanospheres on the surface of PME (**Figure 2B**), indicating successful growth of DA on the ECN surface. Subsequently, we used a Malvern particle size analyser to measure the zeta potential and particle size of PME (**Figure 2C** and **D**). It was found that after encapsulation with PDA, the zeta potential of ECN shifted to a negative value (from –17.66 ± 0.62 mV to –24.2 ± 1.14 mV), and the particle size was increased (from 980 ± 65 nm to 1140 ± 72 nm). Then, ultraviolet-visible spectroscopy was used to detect the loading of MET. After MET was encapsulated, its characteristic absorption peak exhibited a red shift of 13 nm (**Additional Figure 2**). These data suggested that PME was

successfully prepared. Next, we tested the stability of PME in different buffers, and results were shown in **Figure 2E**. In PBS or Tris-HCl, there was no significant change in the particle size of PME within 30 minutes, while in 10% foetal bovine serum, the particle size was gradually decreased. After 30 minutes, the particle size of PME reduced in all buffers, probably due to the growth of ECN causing the disruption of surface PDA film.[28, 29]

We then examined the drug release behaviour of PME. As shown in **Figure 2F**, in Tris-HCl, PME exhibited a slow drug release behaviour, attributing to the stable existence of the PDA film in Tris-HCl. Nevertheless, in all buffers, PME release was surpassed 50% at the 40 minutes, likely attributable to the same factor that facilitate ECN growth as shown in **Figure 2E**, suggesting that PME can effectively deliver drugs within the tumour microenvironment. Considering the photothermal properties of PME, we used a thermal imaging camera to evaluate its photothermal performance. As the concentration of PME increased, concentration-dependent photothermal properties were exhibited (**Figure 2G**). Subsequently, we tested different concentrations and illumination times of PME. As increasing concentration and illumination time, PME produced a strong photothermal effect. The photothermal ability of PME shows a dependence on both irradiation time and concentration (**Figure 2H**). Finally, we subjected PME to repeated irradiation and recorded the temperature increase process. As shown in **Figure 2I**, after repeated laser irradiation, PME still exhibited excellent photothermal capability. This data indicating PME has an excellent viability of photothermal capability.

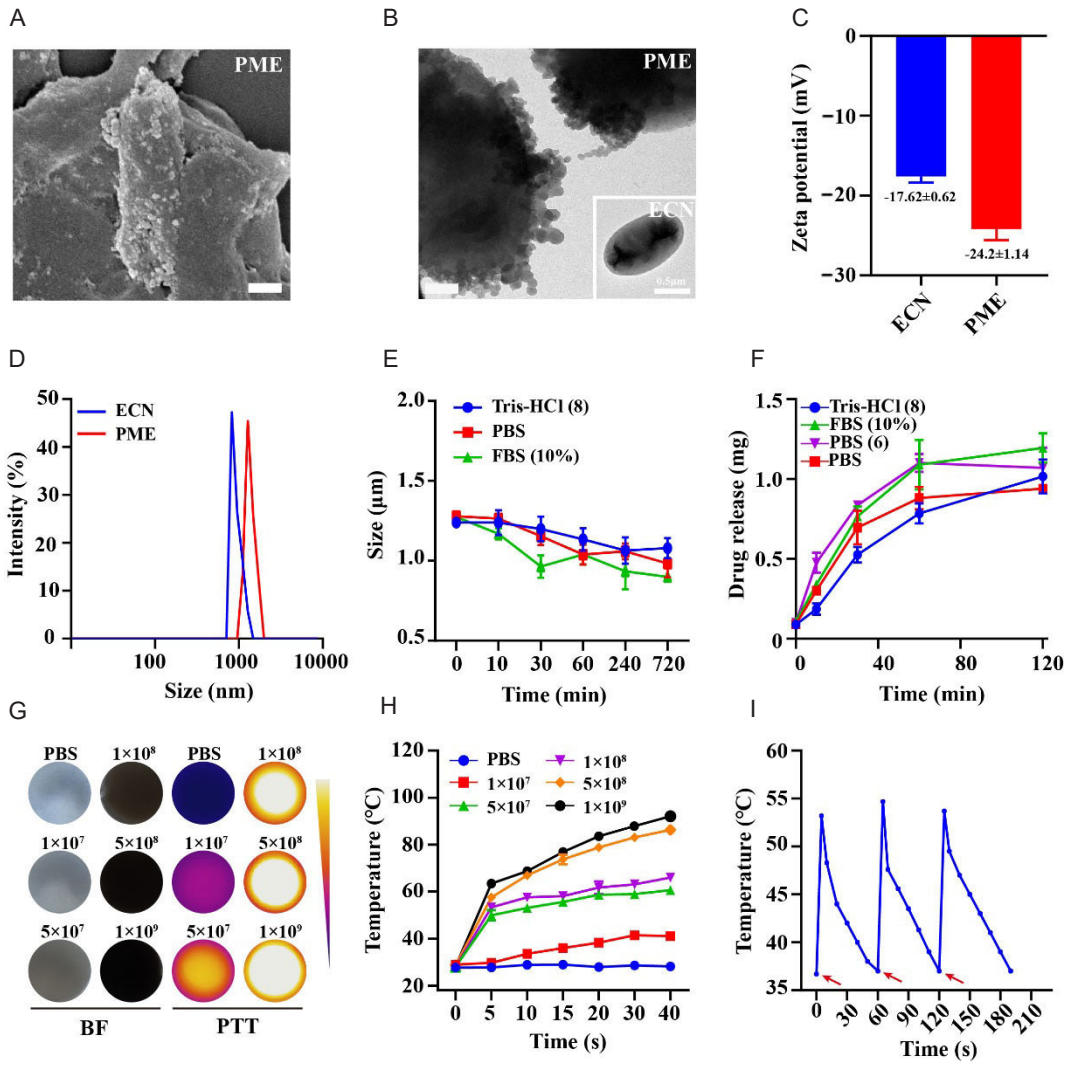

Figure 2. Characterisation of the PME. (A) Representative SEM image of the prepared PME. Scale bar: 200 nm. (B) Representative TEM image of the prepared PME. Scale bar: 200 nm. (C) Zeta potential of ECN and PME (n = 3). (D) The size of ECN, and PME by DLS (n = 3). (E) The stable of PME in various buffer by DLS (n = 3). (F) Release of MET from PME in various buffers (n = 3). (G, H) Thermal images and temperature variation of different concentrations of PME (calculated by ECN) exposed to 0.5 W/cm² laser (n = 3). (I) Repeated irradiation performance of PME. The red arrow indicates irradiation. Data are demonstrated as mean ± SD. BF: bright field; DLS: dynamic light scattering; ECN: *Escherichia coli* Nissle 1917; FBS: foetal bovine serum; MET: metformin; PBS: phosphate buffered saline; PDA: polydopamine; PME: PDA@MET@ECN; PTT: photothermal therapy; SEM: scanning electron microscope; TEM: transmission electron microscope.

PME inhibits the PD-L1 expression in CT26 cells

The heat generated by PTT can scorch tumour cells at the tumour site and induce their immunogenic cell death.[30] Based on the excellent photothermal properties of PME, we hypothesised that it could effectively induce CRT expression in CT26 cells. As shown in **Figure 3A**, compared to the PBS and PBS + laser treatment groups, the PM and PE treatment groups exhibited weak red fluorescence. After treatment with PM + laser and PME + laser, CT26 cells displayed strong red fluorescence. This is due to the heat generated by PDA under 808 nm laser irradiation, which scorches tumour cells and induces CRT expression. Interestingly, PME also produced a significant amount of red fluorescence without laser treatment, likely due to the rapid proliferation of ECN, which deprived the cells of nutrients, leading to cell death.[16] The inflammation caused by PTT induces immune cells to secrete IFN-γ, which can elevate PD-L1 protein expression on the tumour cell surface via the NF-κB pathway. High PD-L1 expression on the tumour surface can inhibit immune cell activity, allowing tumour cells to evade immune attacks and promote metastasis. MET, a specific medication for the treatment of type 2 diabetes, can inhibit PD-L1 expression via the AMPK pathway.[10] We then used western blotting to detect PD-L1 expression in tumour cells after various treatment. As shown in **Figure 3B**, treatments with PM, PM + laser, PME, and PME + laser significantly inhinited PD-L1 expression in CT26 cells, demonstrating that PME has the ability of inhibition PD-L1 expression in CT26 cells.

Finally, we assessed the cytotoxicity of PME. As shown in **Figure 3C** and **D**, without light exposure, PM exhibited minimal cytotoxicity due to its good biocompatibility. However, at concentrations of 5×10^6 cfu, both PE (IC50: 4.6×10^6 cfu) and PME (IC50: 4.2×10^6 cfu) inhibited CT26 cell growth, possibly due to the rapid proliferation of ECN leading to cell death from nutrient deprivation.[16] Under 808 nm laser irradiation, PM (IC50: 0.26 mg/mL), PE (IC50: 2.3×10^6 cfu), and PME (IC50: 2.2×10^6 cfu) effectively inhibited tumour cell growth, indicating that PDA coated on ECN retains good photothermal therapeutic effects. The Calcein/PI staining analysis was further performed, and the results are shown in **Figure 3E**. PME + laser significantly induced tumour cell death, demonstrating that PME has a strong PTT effect under light exposure.

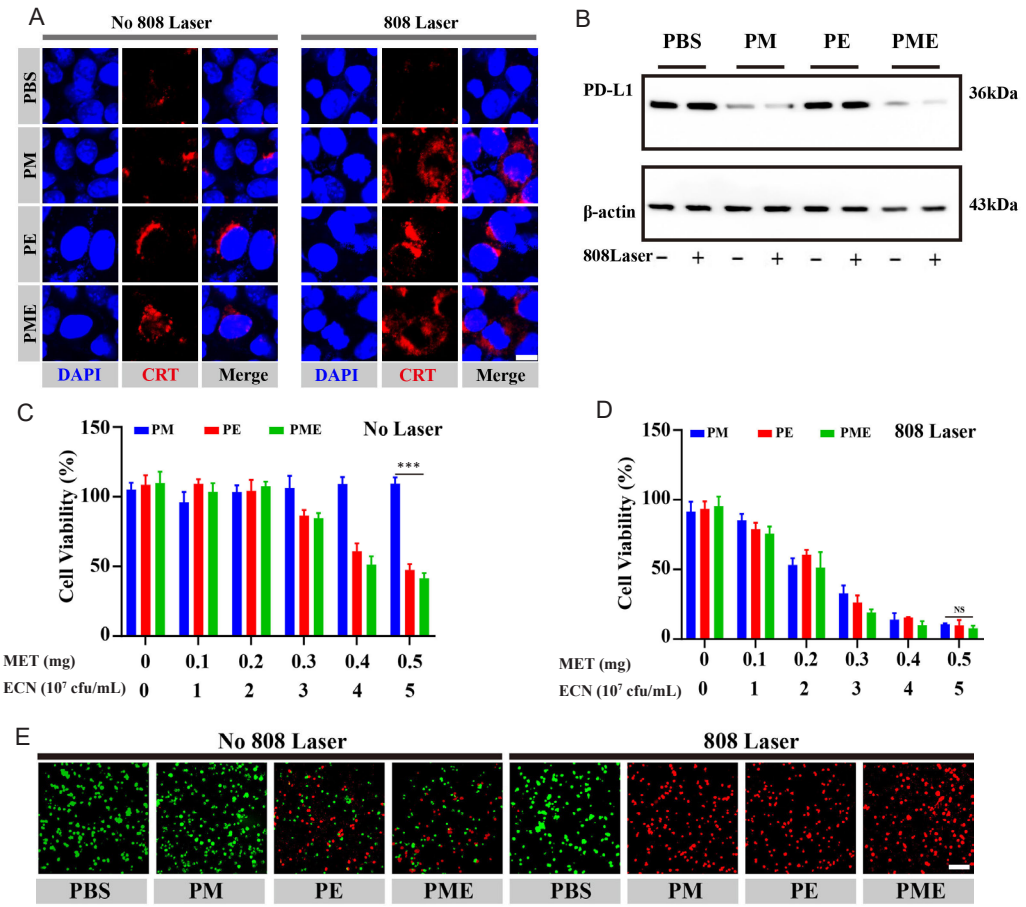

Figure 3. PME inhibits PD-L1 expression *in vitro*. (A) Representative immunofluorescence images of CRT exposure after various treatments. Scale bar: 10 μm. (B) PME inhibited the expression of PD-L1 protein in CT26 tumour cells after 24-hour treatments. (C, D) Cell viability of CT26 tumour cells detected by Cell Counting Kit-8 assay ($n = 3$). (E) Representative images of CT26 tumour cells after various treatments. Scale bar: 50 μm. Data are demonstrated as mean ± SD. ***$P < 0.001$ (one-way analysis of variance). CRT: calprotectin; DAPI: 4′,6-diamidino-2-phenylindole; ECN: *Escherichia coli* Nissle 1917; MET: metformin; NS: no significant difference; PBS: phosphate buffered saline; PD-L1: programmed cell death ligand 1; PDA: polydopamine; PME: PDA@MET@ECN.

Pharmacokinetics and biodistribution of PME *in vivo*

ECN inherent tumour-targeting capability has garnered increasing attention in the field of tumour therapy. First, an *in vivo* imaging system was used to detect the distribution of PME in the body. To facilitate the observation of ECN distribution *in vivo*, we used the near-infrared fluorescent molecule ICG instead of MET, referred to as PDA@ICG or PDA@ICG@ECN. As shown in **Figure 4A** and **B** (red fluorescence of ICG was used to replace MET for *in vivo* imaging system), after tail vein injection, PIE primarily accumulated in the liver (0.5 hour). PIE gradually accumulated at the tumour site (from 12 hours to 24 hours), with the fluorescence intensity at the tumour site peaking at 12 hours post-injection. After 12 hours, the major organs (heart, liver, spleen, lungs, kidneys) and tumour tissues of the mice were collected. The distribution of MET in the organs is shown in **Figure 4C**. Compared to the PM treatment group, PME specifically accumulated at the tumour site, reducing the clearance of the drug by the liver and kidneys. We further confirmed the predominant distribution of ECN at the tumour site using the plate coating method (**Figure 4D**). Subsequently, we tested the photothermal performance of PME *in vivo*. Compared to the PBS treatment group, the injection of PME followed by excitation with an 808 nm laser resulted in an increase in temperature at the tumour site. The temperature changes showed a time-dependent upward trend (**Figure 4E**). The photothermal imaging of the tumour site is shown in **Figure 4F**. These findings suggest that PME not only effectively targets tumours but also demonstrates significant photothermal effects, making it a promising candidate for enhanced tumour therapy.

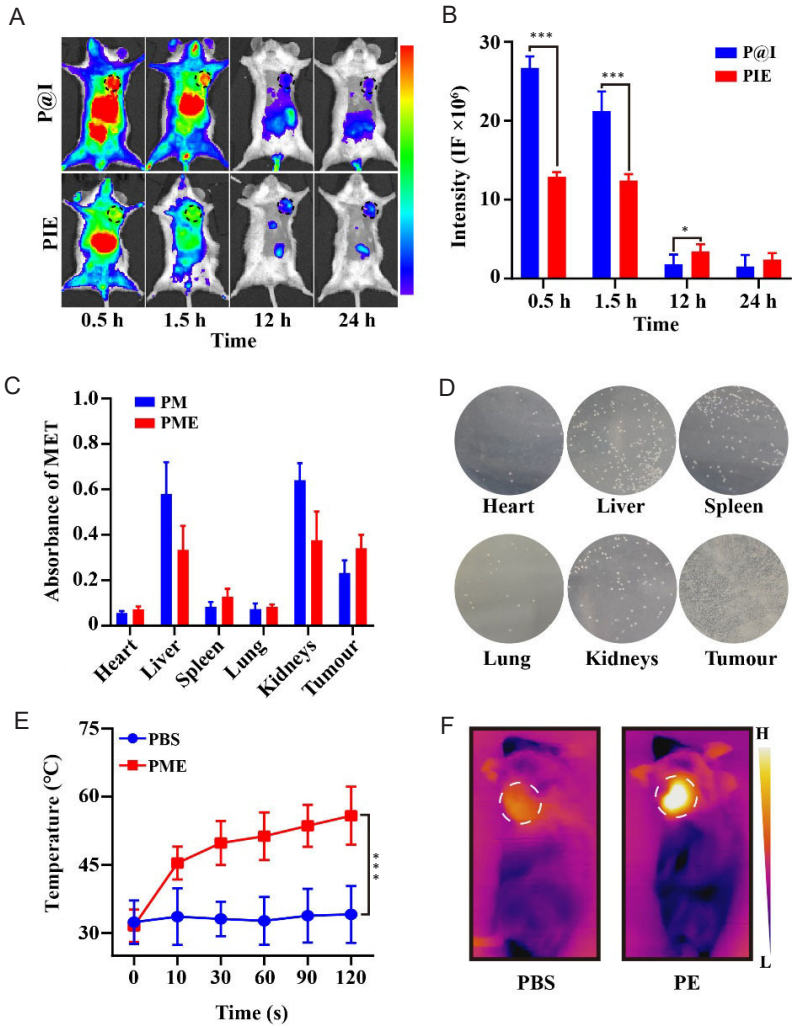

Figure 4. Pharmacokinetics and biodistribution of PME *in vivo*. (A) Real-time NIR fluorescence images of the CT26 tumour-bearing mice after intravenous injection of P@I or PIE . (B) Quantitative analysis of fluorescence intensity at tumour site (n = 3). (C) Quantification of MET concentration in tumours and normal tissues at 24 hours after PM or PME treatments (n = 3). (D) The distribution of ECN in tumours and normal tissues at 24 hours after PME treatments. (E) The temperature in CT26 tumours after NIR laser irradiation (n = 3). The mice were pre-treated with PME for 24 hours. (F) Representative *in vivo* infrared thermal images of CT26 tumours irradiated 10 seconds at 0.5 W/cm^2 for twice at 24 hours. Data are demonstrated as mean ± SD. *P < 0.05, ***P < 0.001 (one-way analysis of variance). ECN: *Escherichia coli* Nissle 1917; H: high; ICG: indocyanine green; IF: intensity of fluorescence; L: low; MET: metformin; P@I: PDA@ICG; PDA: polydopamine; PBS: phosphate buffered saline; PIE: PDA@ICG@ECN; PE: PDA@ECN; PM: PDA@MET; PME: PDA@MET@ECN.

PME inhibits the growth of CT26 tumour cells *in vivo*

PME has been shown to inhibit tumour cell growth through PTT *in vitro* (**Figure 3**). To further validate its therapeutic efficacy *in vivo*, we employed the CT26 murine tumour model for pharmacodynamic testing. As shown in **Figure 5A**, when the tumour volume reached 100 mm³, the mice were administered with PME via tail intravenous injection, and 24 hours later, the mice received 808 nm laser treatment. The tumour volume changes over 14 days are depicted in **Figure 5B–I**. There was no significant difference in tumour volume between the PBS groups, with or without laser irradiation, indicating that 808 nm laser alone had no effect on tumour growth. However, the PM and PE groups inhibited tumour cell growth, but the inhibitory effect was lower than that observed in the PME and PME + laser treatment groups. This may be due to PME enhancing the PTT effect at the tumour site. Interestingly, PME treatment alone also effectively suppressed tumour growth, potentially due to the intrinsic anti-tumour properties of ECN, such as nutrient competition at the tumour site and the secretion of bacterial toxins. The synergistic effect between ECN and PM resulted in significant anti-tumour activity of PME, even in the absence of laser irradiation. The tumour tissue weight, shown in **Figure 5J**, further confirmed that PME under laser irradiation effectively inhibited tumour growth. After 14 days of treatment, tumour tissues were collected and are displayed in **Additional Figure 3**. Compared to the PBS group, the tumour size in the PBS + laser treatment group was similar to that of the PBS group. Although the PM, PM + laser, and PE groups suppressed tumour growth, their therapeutic efficacy was still inferior to that of the PE + laser and PME + laser treatment groups. This further indicates that PME combined with laser can effectively inhibit tumour cell growth *in vivo*.

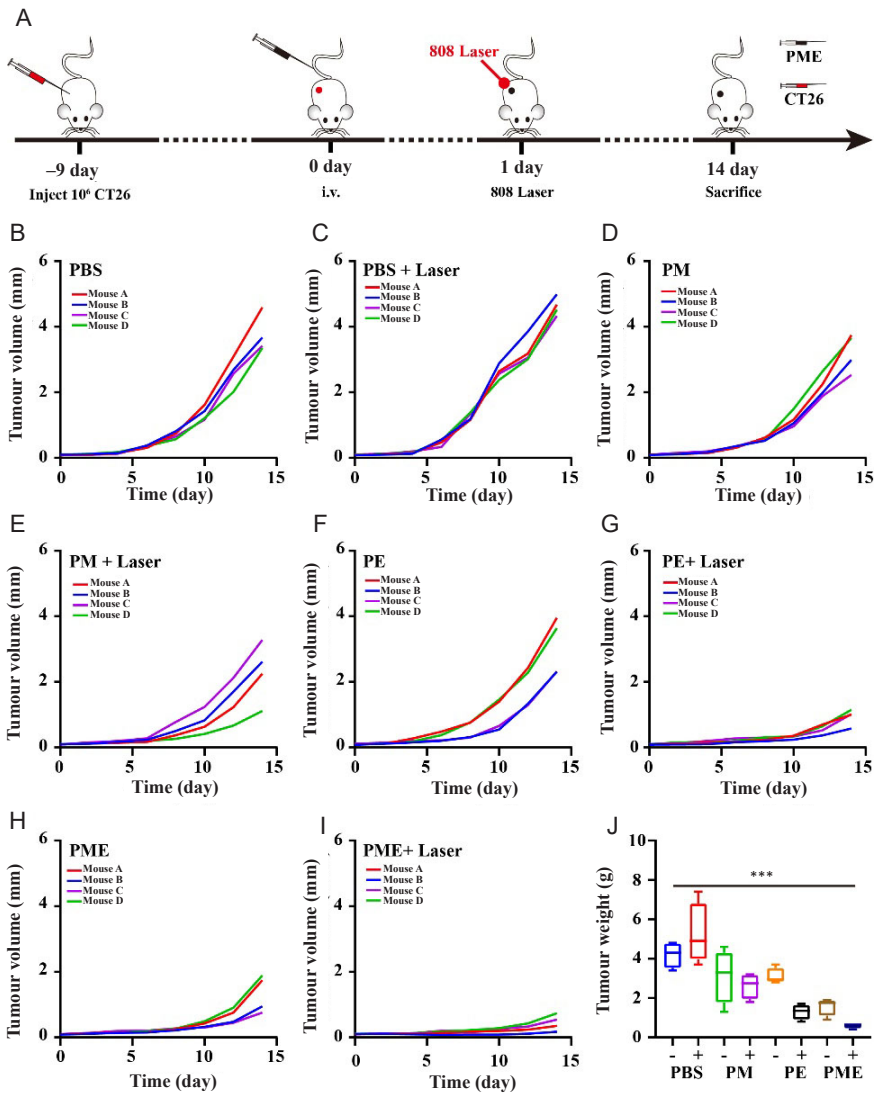

Figure 5. *In vivo* anti-tumour efficacy of PME-mediated PTT in CT26 tumours. (A) Schematic diagram of CT26 tumour experimental design. (B-I) Tumour growth curves of CT26 tumour-bearing mice after the various treatments ($n = 4$). (J) Weights of excised distal CT26 tumours ($n = 4$). Data are demonstrated as mean ± SD. ***$P < 0.001$ (one-way analysis of variance). ECN: *Escherichia coli* Nissle 1917; i.v.: intravenous injection; MET: metformin; PBS: phosphate buffered saline; PDA: polydopamine; PE: PDA@ECN; PM: PDA@MET; PME: PDA@MET@ECN; PTT: photothermal therapy.

PME induces CRT expression *in vivo* and recruits immune cell infiltration

PTT can induce immunogenic cell death in tumour cells. To further elucidate the anti-tumour mechanism of PME *in vivo*, we first examined the expression of the immunogenic cell death marker CRT in tumour tissues following PME treatment. As shown in **Figure 6A**, compared to other treatment groups, the PM + laser, PE + laser, and PME + laser groups exhibited strong green fluorescence for CRT, indicating tumour cell immunogenicity death due to the heat generated by the excellent photothermal properties of PDA. Interestingly, CRT expression was more than three times higher in the PE + laser and PME + laser groups than in the PM+Laser group. This difference could be attributed to the easier capture of PM nanoparticles by the liver's reticuloendothelial system, resulting in lower accumulation of PM at the tumour site compared to the PE and PME groups.

Subsequently, we used immunohistochemistry to detect the expression of PD-L1 in tumour tissues, with the results shown in **Figure 6B**. After treatment with PBS, PBS + laser, PE, and PE + laser, the tissue sections displayed strong gray staining, indicating that PD-L1 expression was unaffected. However, PD-L1 expression was suppressed following treatment with PM, PM + laser, PME, and PME + laser. The strong PD-L1 suppression in the PME and PME+Laser groups was likely due to the active tumour-targeting ability of ECN. This effectively reversed the formation of the immunosuppressive tumour microenvironment.

Considering PME's strong PTT and PD-L1 suppression capabilities, we next assessed immune cell infiltration at the tumour site. As illustrated in **Figure 6C**, after PME + Laser treatment, a large number of immune cells were recruited to infiltrate the tumour, leading to increased numbers of $CD4^+$ (green) and $CD8^+$ (red) T lymphocytes in the tumour microenvironment, thereby achieving a synergistic PTT-immune therapeutic effect. Ki67, a marker of cell proliferation, was used to evaluate the proliferation capacity of tumour cells following various treatments, with immunofluorescence results shown in **Figure 6D–F**. The PBS group exhibited strong red fluorescence, indicating rapid tumour cell growth. The PM group displayed similar fluorescence intensity of PBS, suggesting that PM alone could not inhibit tumour growth in the absence of laser irradiation. In contrast, the PE + laser and PME + laser groups showed significant inhibitory effects, demonstrating the synergistic anti-tumour capacity of ECN and PTT.

Since ECN can act as an antigen to recruit immune cell infiltration at the tumour site, we subsequently used enzyme-linked immunosorbent assay to measure levels of tumour necrosis factor-α in mouse blood, as shown in **Figure 6G**. Following treatment with PE, PE + laser, PME, and PME + laser, an strong inflammatory response was induced, resulting in higher levels of tumour necrosis factor-α compared to other groups, which effectively inhibited tumour growth.

Finally, we performed haematoxylin and eosin staining to observe the morphology of tumour tissues. The results indicated that tumour cells in the PME + laser group exhibited nuclear fragmentation, cytoplasmic dissolution, and disrupted cellular structures. These findings demonstrate that PME under laser irradiation can effectively induce immunogenic cell death in tumour cells, recruit T lymphocytes for tumour infiltration, and achieve synergistic anti-tumour effects through PTT combined with immunotherapy.

In vivo safety evaluation of PME

To demonstrate the biosafety of PME, we first collected blood samples from mice 14 days after treatment to assess the functional stability of their liver and kidneys. As shown in **Figure 7A** and **B**, no significant differences were observed in liver function markers, aspartate aminotransferase, and alanine aminotransferase, compared to the PBS group. Similarly, the kidney function indicators, creatinine and blood urea nitrogen, also showed no significant differences and remained within the normal range (**Figure 7C** and **D**). Additionally, the body weight of the mice did not show any significant changes during the 14-day treatment period (**Additional Figure 4**).

Subsequently, we performed haematoxylin and eosin staining on major organs, including the heart, liver, spleen, lungs, and kidneys. As shown in **Figure 7E**, unlike the tumour sections after treatment (**Figure 6H**), the tissue sections of major organs from all treatment groups exhibited intact cellular structures with clear cellular boundaries. Furthermore, the cytoplasmic staining was uniformly distributed in red, indicating no visible damage to the major organs following PME treatment. These results indicate that PME demonstrates outstanding biocompatibility and is safe for application in *in vivo* tumour therapy.

Discussion

ECN has a K5:O6 capsule on its surface, making it susceptible to clearance by immune cells in the bloodstream.[17, 31] It is the only strain of *E. coli* that is non-pathogenic in humans. Due to its facultative anaerobic nature, ECN can easily colonise at tumour sites, penetrating deep into the tumour core.[32, 33] Therefore, ECN-based cancer therapy strategies have gained widespread attention. In this study, ECN was used as the chassis cell, with DA self-assembling on its surface to create a PTT-capable, tumour-targeting living material for the treatment of solid tumours. Previous research has shown that PTT triggers high expression of IFN-γ at tumour sites, which in turn stimulates PD-L1 protein expression on tumour cells, allowing them to evade immune surveillance.[10] To address this issue, we successfully encapsulated a PD-L1 inhibitor (MET) on the surface of ECN, creating the PME living material. PME not only exhibited excellent photothermal properties but also effectively suppressed PD-L1 expression in CT26 cells *in vitro* (**Figures 2** and **3**). Due to ECN tumour-targeting ability, PME rapidly colonised at tumour sites and displayed strong photothermal effects under 808 nm laser irradiation (**Figures 4** and **5**). In CT26 tumour model, PME+Laser treatment significantly increased CRT expression and inhibited PD-L1 expression in tumour tissues. PTT induced a large infiltration of immune cells into the tumour, stimulating inflammatory processes and elevating tumour necrosis factor-α and IFN-γ expression levels (**Figure 6**). This intervention significantly inhibited the growth of CT26 cells in mice, resulting in an inhibition rate exceeding 80%. Furthermore, PME demonstrated excellent biocompatibility, making it suitable for *in vivo* anti-tumour research (**Figure 7**).

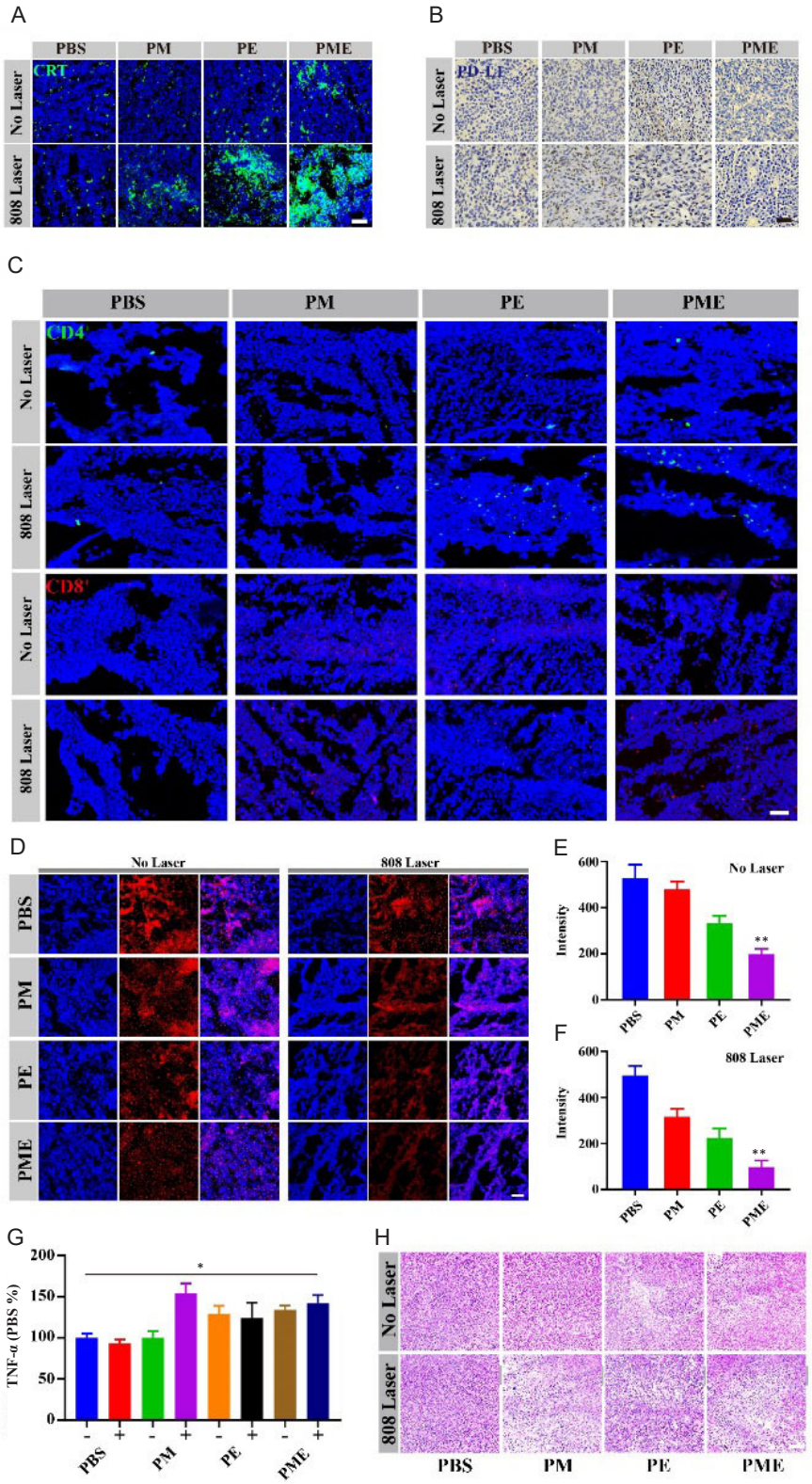

Figure 6. Anti-tumour efficacy of PME in CT26 tumour bear mice *in vivo*. (A) Representative image of CRT staining after various treatments. Scale bar: 100 μm. (B) Representative image of PD-L1 staining after various treatments. Scale bar: 50 μm. (C) Quantification of $CD4^+$ and $CD8^+$ T cells in representative images. Scale bar: 100 μm. (D–F) Quantification and representative images of Ki67 staining. Scale bar: 100 μm. (G) The level of TNF-α in the serum after different treatments. – represents no laser, and represents laser. (H) Representative images of H&E staining of tumour slice after various treatments. Scale bar: 100 μm. Data are demonstrated as mean ± SD. $^*P < 0.05$, $^{**}P < 0.01$ (one-way analysis of variance). CRT: calprotectin; ECN: *Escherichia coli* Nissle 1917; H&E: haematoxylin and eosin; MET: metformin; PBS: phosphate buffered saline; PD-L1: programmed cell death ligand 1; PDA: polydopamine; PE: PDA@ECN; PM: PDA@MET; PME: PDA@MET@ECN; TNF-α: tumour necrosis factor-α.

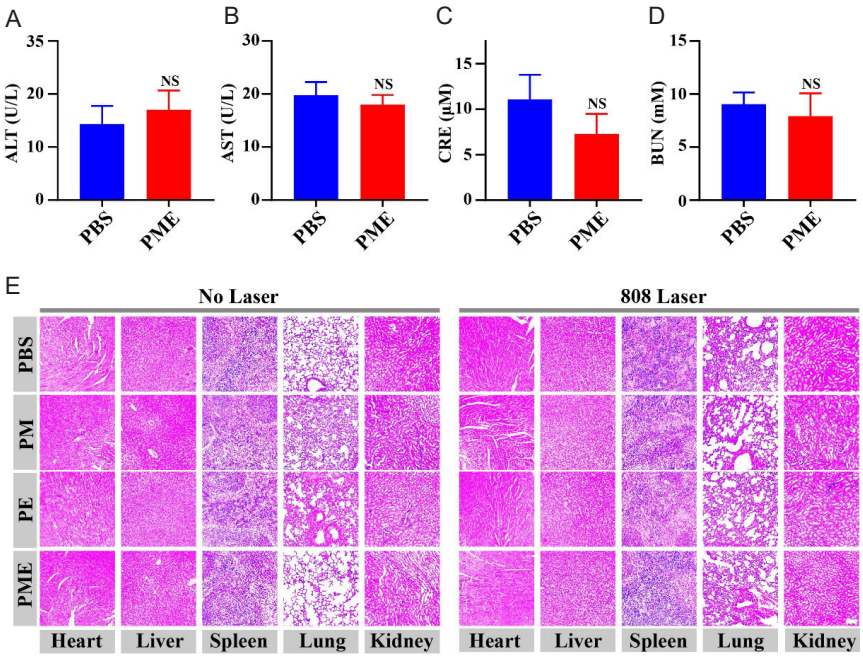

Figure 7. Biosafety of PME in BALB/c mice. (A, B) Serum AST and ALT levels ($n = 3$). (C, D) Serum CRE and BUN levels ($n = 3$). (E) H&E staining images of the major organs on day 14. Scale bar: 100 μm. The data are presented as the means ± SD, and were analysed by two-tail Student's *t*-test. ALT: alanine aminotransferase; AST: aspartate aminotransferase; BUN: blood urea nitrogen; CRE: creatinine; ECN: *Escherichia coli* Nissle 1917; H&E: haematoxylin and eosin; MET: metformin; NS: no significant difference; PDA: polydopamine; PBS: phosphate buffered saline; PE: PDA@ECN; PM: PDA@MET; PME: PDA@MET@ECN.

Although ECN has garnered increasing attention as a drug delivery vector in cancer treatment, its use as a live bacterium for direct injection carries potential risks, such as genotoxicity and cytokine storms.[34, 35] Current synthetic biology techniques are working on genetically engineering ECN strains with features like self-lysis, quorum sensing, and nutrient auxotrophy to enhance its safety.[36, 37] However, these approaches are still in early stages of research. Overall, compared to traditional nanomaterials, ECN-based drug delivery strategies offer richer functionalities (such as gene modification for exogenous protein expression) and active tumour targeting. Therefore, ECN-based living delivery strategies represent a highly promising approach for cancer treatment.

Author contributions

NJ: Investigation, writing-original draft; MJ: data analysis; JC: experimental operation; AM: draft writing and editing; XY: platform support and supervision for cell experiment; YZ: platform support and supervision; JQ: platform support and supervision for writing; JH: supervision, funding acquisition, writing- review & editing. All authors have read and approved the final version of the manuscript.

Financial support

This study was supported by the National Key Research and Development Program of China (No. 2020YFA0908900), the Natural Science Foundation of Shanghai (No. 22ZR1416000), and the Open Funding Project of State Key Laboratory of Microbial Metabolism (No. MMLKF24-01).

Acknowledgement

We thank Professor Chengcheng Liu (Xi'an Jiao Tong University) and Jianliang Shen (Wenzhou Medical University) for providing ECN and murine colon cancer CT26 cells, respectively. We also thank the Research Center of Analysis and Test in East China University of Science and Technology for data collection and characterisation. We thank Professor Fen'er Chen (Jiangxi Normal University) for the comments.

Conflicts of interest statement

The authors declare no conflicts of interest.

Additional files

Additional Figure 1: *Representative SEM image of the prepared ECN.*

Additional Figure 2: *Characteristic absorption peak of MET and PME by ultraviolet-visible spectroscopy.*

Additional Figure 3: *The appearance of CT26 tumours.*

Additional Figure 4: *Body weight during the different treatments.*

1. Li, X.; Yong, T.; Wei, Z.; Bie, N.; Zhang, X.; Zhan, G.; Li, J.; Qin, J.; Yu, J.; Zhang, B.; Gan, L.; Yang, X. Reversing insufficient photothermal therapy-induced tumor relapse and metastasis by regulating cancer-associated fibroblasts. *Nat Commun.* **2022,** *13*, 2794.
2. Ji, B.; Wei, M.; Yang, B. Recent advances in nanomedicines for photodynamic therapy (PDT)-driven cancer immunotherapy. *Theranostics.* **2022,** *12*, 434-458.
3. Overchuk, M.; Weersink, R. A.; Wilson, B. C.; Zheng, G. Photodynamic and photothermal therapies: synergy opportunities for nanomedicine. *ACS Nano.* **2023,** *17*, 7979-8003.
4. Jiang, N.; Zhou, Z.; Xiong, W.; Chen, J.; Shen, J.; Li, R.; Ye, R. Tumor microenvironment triggered local oxygen generation and photosensitizer release from manganese dioxide mineralized albumin-ICG nanocomplex to amplify photodynamic immunotherapy efficacy. *Chin Chem Lett.* **2021,** *32*, 3948-3953.
5. Peng, D.; Fu, M.; Wang, M.; Wei, Y.; Wei, X. Targeting TGF-β signal

transduction for fibrosis and cancer therapy. *Mol Cancer.* **2022,** *21*, 104.

6. Bagrov, D. V.; Adlerberg, V. V.; Skryabin, G. O.; Nikishin, II; Galetsky, S. A.; Tchevkina, E. M.; Kirpichnikov, M. P.; Shaitan, K. V. AFM-TEM correlation microscopy and its application to lipid nanoparticles. *Microsc Res Tech.* **2023,** *86*, 781-790.
7. Dong, X.; Zang, C.; Sun, Y.; Zhang, S.; Liu, C.; Qian, J. Hydroxyapatite nanoparticles induced calcium overload-initiated cancer cell-specific apoptosis through inhibition of PMCA and activation of calpain. *J Mater Chem B.* **2023,** *11*, 7609-7622.
8. Liu, K.; Cheng, M.; Huang, H.; Yu, H.; Zhao, S.; Zhou, J.; Tie, D.; Wang, J.; Pan, P.; Chen, J. Abalone shell-derived Mg-doped mesoporous hydroxyapatite microsphere drug delivery system loaded with icariin for inducing apoptosis of osteosarcoma cells. *Biomater Transl.* **2024,** *5*, 185-196.
9. Xi, Y.; Chen, L.; Tang, J.; Yu, B.; Shen, W.; Niu, X. Amplifying "eat me signal" by immunogenic cell death for potentiating cancer immunotherapy. *Immunol Rev.* **2024,** *321*, 94-114.
10. Xiong, W.; Qi, L.; Jiang, N.; Zhao, Q.; Chen, L.; Jiang, X.; Li, Y.; Zhou, Z.; Shen, J. Metformin liposome-mediated PD-L1 downregulation for amplifying the photodynamic immunotherapy efficacy. *ACS Appl Mater Interfaces.* **2021,** *13*, 8026-8041.
11. Kim, Y.; Vagia, E.; Viveiros, P.; Kang, C. Y.; Lee, J. Y.; Gim, G.; Cho, S.; Choi, H.; Kim, L.; Park, I.; Choi, J.; Chae, Y. K. Overcoming acquired resistance to PD-1 inhibitor with the addition of metformin in small cell lung cancer (SCLC). *Cancer Immunol Immunother.* **2021,** *70*, 961-965.
12. Hughes, T.; Klairmont, M.; Sharfman, W. H.; Kaufman, H. L. Interleukin-2, Ipilimumab, and anti-PD-1: clinical management and the evolving role of immunotherapy for the treatment of patients with metastatic melanoma. *Cancer Biol Ther.* **2021,** *22*, 513-526.
13. Yin, S.; Chen, Z.; Chen, D.; Yan, D. Strategies targeting PD-L1 expression and associated opportunities for cancer combination therapy. *Theranostics.* **2023,** *13*, 1520-1544.
14. Han, Y.; Wang, L.; Cao, K.; Zhou, J.; Zhu, Y.; Hou, Y.; Lu, Y. In Situ TEM Characterization and modulation for phase engineering of nanomaterials. *Chem Rev.* **2023,** *123*, 14119-14184.
15. Kong, N.; Ma, H.; Pu, Z.; Wan, F.; Li, D.; Huang, L.; Lian, J.; Huang, X.; Ling, S.; Yu, H.; Yao, Y. De novo design and synthesis of polypeptide immunomodulators for resetting macrophage polarization. *Biodes Res.* **2023,** *5*, 0006.
16. Huang, X.; Pan, J.; Xu, F.; Shao, B.; Wang, Y.; Guo, X.; Zhou, S. Bacteria-based cancer immunotherapy. *Adv Sci (Weinh).* **2021,** *8*, 2003572.
17. Lin, D.; Feng, X.; Mai, B.; Li, X.; Wang, F.; Liu, J.; Liu, X.; Zhang, K.; Wang, X. Bacterial-based cancer therapy: an emerging toolbox for targeted drug/gene delivery. *Biomaterials.* **2021,** *277*, 121124.
18. Dong, X.; Wu, W.; Pan, P.; Zhang, X. Z. Engineered living materials for advanced diseases therapy. *Adv Mater.* **2023**, e2304963.
19. Li, J.; Xia, Q.; Guo, H.; Fu, Z.; Liu, Y.; Lin, S.; Liu, J. Decorating bacteria with triple immune nanoactivators generates tumor-resident living immunotherapeutics. *Angew Chem Int Ed Engl.* **2022,** *61*, e202202409.
20. Luo, H.; Wu, F.; Wang, X.; Lin, S.; Zhang, M.; Cao, Z.; Liu, J. Encoding bacterial colonization and therapeutic modality by wrapping with an adhesive drug-loadable nanocoating. *Mater Today.* **2023,** *62*, 98-110.
21. Liu, Y.; Zhang, M.; Wang, X.; Yang, F.; Cao, Z.; Wang, L.; Liu, J. Dressing bacteria with a hybrid immunoactive nanosurface to elicit dual anticancer and antiviral immunity. *Adv Mater.* **2023,** *35*, e2210949.
22. Sun, R.; Liu, M.; Lu, J.; Chu, B.; Yang, Y.; Song, B.; Wang, H.; He, Y. Bacteria loaded with glucose polymer and photosensitive ICG silicon-nanoparticles for glioblastoma photothermal immunotherapy. *Nat Commun.* **2022,** *13*, 5127.
23. Wang, Y.; Zhou, S. K.; Wang, Y.; Lu, Z. D.; Zhang, Y.; Xu, C. F.; Wang, J. Engineering tumor-specific gene nanomedicine to recruit and activate T cells for enhanced immunotherapy. *Nat Commun.* **2023,** *14*, 1993.
24. Peng, R.; Ba, F.; Li, J.; Cao, J.; Zhang, R.; Liu, W. Q.; Ren, J.; Liu, Y.; Li, J.; Ling, S. Embedding living cells with a mechanically reinforced and functionally programmable hydrogel fiber platform. *Adv Mater.* **2023,** *35*, e2305583.
25. Zhao, R.; Li, Z.; Sun, Y.; Ge, W.; Wang, M.; Liu, H.; Xun, L.; Xia, Y. Engineered Escherichia coli Nissle 1917 with urate oxidase and an oxygen-recycling system for hyperuricemia treatment. *Gut Microbes.* **2022,** *14*, 2070391.
26. Chen, W.; Wang, Y.; Qin, M.; Zhang, X.; Zhang, Z.; Sun, X.; Gu, Z. Bacteria-driven hypoxia targeting for combined biotherapy and photothermal therapy. *ACS Nano.* **2018,** *12*, 5995-6005.
27. Li, J.; Hou, W.; Lin, S.; Wang, L.; Pan, C.; Wu, F.; Liu, J. Polydopamine nanoparticle-mediated dopaminergic immunoregulation in colitis. *Adv Sci (Weinh).* **2022,** *9*, e2104006.
28. Wang, X.; Lin, S.; Wang, L.; Cao, Z.; Zhang, M.; Zhang, Y.; Liu, R.; Liu, J. Versatility of bacterial outer membrane vesicles in regulating intestinal homeostasis. *Sci Adv.* **2023,** *9*, eade5079.
29. Lin, S.; Wu, F.; Zhang, Y.; Chen, H.; Guo, H.; Chen, Y.; Liu, J. Surface-modified bacteria: synthesis, functionalization and biomedical applications. *Chem Soc Rev.* **2023,** *52*, 6617-6643.
30. Yang, J. K.; Kwon, H.; Kim, S. Recent advances in light-triggered cancer immunotherapy. *J Mater Chem B.* **2024,** *12*, 2650-2669.
31. Lou, X.; Chen, Z.; He, Z.; Sun, M.; Sun, J. Bacteria-mediated synergistic cancer therapy: small microbiome has a big hope. *Nanomicro Lett.* **2021,** *13*, 37.
32. Chen, H.; Lei, P.; Ji, H.; Yang, Q.; Peng, B.; Ma, J.; Fang, Y.; Qu, L.; Li, H.; Wu, W.; Jin, L.; Sun, D. Advances in Escherichia coli Nissle 1917 as a customizable drug delivery system for disease treatment and diagnosis strategies. *Mater Today Bio.* **2023,** *18*, 100543.
33. Cao, Z.; Liu, J. Bacteria and bacterial derivatives as drug carriers for cancer therapy. *J Control Release.* **2020,** *326*, 396-407.
34. Zou, S.; Jie, H.; Han, X.; Wang, J. The role of neutrophil extracellular traps in sepsis and sepsis-related acute lung injury. *Int Immunopharmacol.* **2023,** *124*, 110436.
35. Xiong, D.; Song, L.; Chen, Y.; Jiao, X.; Pan, Z. Salmonella Enteritidis activates inflammatory storm via SPI-1 and SPI-2 to promote intracellular proliferation and bacterial virulence. *Front Cell Infect Microbiol.* **2023,** *13*, 1158888.
36. Gurbatri, C. R.; Lia, I.; Vincent, R.; Coker, C.; Castro, S.; Treuting, P. M.; Hinchliffe, T. E.; Arpaia, N.; Danino, T. Engineered probiotics for local tumor delivery of checkpoint blockade nanobodies. *Sci Transl Med.* **2020,** *12*, eaax0876.
37. Liu, L.; Helal, S. E.; Peng, N. CRISPR-Cas-based engineering of probiotics. *Biodes Res.* **2023,** *5*, 0017.

Received: October 30, 2024
Revised: November 22, 2024
Accepted: February 25, 2025
Available online: March 25, 2025